Journal of Fluids and Structures (2000) **14,** 1119–1144
doi:10.1006/jfls.2000.0315, available online at http://www.idealibrary.com on IDEAL®

AERODYNAMIC STIFFNESS AND DAMPING EFFECTS IN THE ROTATIONAL GALLOPING OF A RECTANGULAR CROSS-SECTION

B. W. van Oudheusden

Faculty of Aerospace Engineering, Delft University of Technology
P.O. Box 5058, 2600 GB Delft, The Netherlands

(Received 15 June 1999, and in final form 9 May 2000)

The galloping oscillation with a single rotational degree of freedom is investigated for a prismatic beam with a rectangular cross-section. For this particular geometric configuration, the effect of the unsteady aerodynamic forces can be understood as a combination of aerodynamic stiffness and damping terms, with the latter being the most relevant for the instability behaviour. A theoretical prediction of both these effects is made for this type of galloping behaviour, based on a quasi-steady aerodynamic approach. Comparison to experimental results obtained in wind tunnel experiments reveals significant shortcomings of the quasi-steady approach in predicting, in particular, the damping effect. For the stiffness effect, the agreement is much better.

1. INTRODUCTION

1.1. Aerodynamic Damping and Stiffness Effects in Galloping Instabilities

When an oscillating structure is exposed to a steady homogeneous wind field, it experiences a time-varying aerodynamic loading, which is induced by the relative motion between the structure and the surrounding air. The component of the unsteady loading that is in phase with the displacement of the motion can be regarded to act as an aerodynamic stiffness, while the component in phase with the velocity of the motion can be interpreted as an aerodynamic damping. The stiffness affects the frequency and mode shape of the oscillation, with regard to the natural motion of the structure in the absence of aerodynamic forces, while the damping effect determines the stability of the motion, i.e. the possible growth or decay of the oscillation amplitude in time.

In the case of separated flow, which is the situation normally encountered in many civil engineering applications where wind loading dynamics are important, the wind load relations are highly nonlinear with respect to the angle of incidence, and therefore, the amplitude of the motion. This is also relevant for the type of instabilities referred to as galloping (Blevins 1990; Dowell *et al.* 1995) which rely, fundamentally, on the occurrence of negative aerodynamic damping (Parkinson & Smith 1964). Because of the nonlinear nature of the aerodynamic loads, the stability depends on the motion amplitude, and this may result in (multiple) regions of stable and unstable amplitudes, hence leading to (multiple) limit-cycle solutions.

Typically, the analysis of the dynamical behaviour of these galloping problems follows the approach of a weakly nonlinear perturbation of the natural modes (Blevins 1990). The unsteady wind loads are modelled on the basis of a quasi-steady aerodynamic assumption, employing static aerodynamic data measured in the wind tunnel. For galloping oscillations

0889–9746/00/111119 + 26 $35.00/0

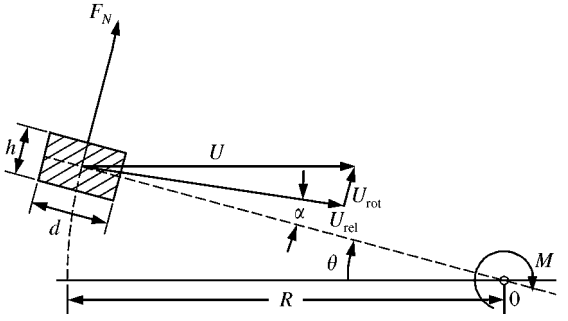

Figure 1. Modelling of one-degree-of-freedom galloping with combined translational and rotational effects (cross-sectional view; rotation axis is at point O; $U_{rot} = R\,\mathrm{d}\theta/\mathrm{d}t$).

with only one degree of freedom (1-dof), changes in the frequency of the oscillation are not very relevant, and the influence of stiffness effects can therefore often be omitted from the analysis.

The subject of our present investigation is the galloping behaviour of the rotational oscillation of a rigid, prismatic beam in a steady, homogeneous cross flow normal to its axis (see Figure 1). With regard to the aeroelastic behaviour of practical structures, the present oscillator can be seen to represent a simplified model of the case where the elastic axis is located downstream of the aerodynamic axis. As shown in earlier studies (Haaker & van Der Burgh 1994; van Oudheusden 1995), this configuration can be seen as an extension of the classical case of cross-flow translational galloping (Parkinson & Smith 1964). In both cases, the relevant aerodynamic force is the normal force component F_N on the beam. However, in contrast to the translational case, there is now a dependence on both the angular displacement and the angular velocity, as is typical for rotational motions. The major motivation for the interest in this specific configuration lies in the fact that, as the rotation arm length R is significantly larger than the typical dimension of the cross-section (for example its depth d), more confidence in the application of the quasi-steady theory can be expected for this type of rotational galloping (van Oudheusden 1995), than for pure torsion with the rotation centre close to the aerodynamic centre of the cross-section (Novak 1971; Nakamura & Mizota 1975; Blevins 1990). The validity of the quasi-steady approach is further improved by the very low natural frequency (circa 0·6 Hz), chosen in order to achieve very low values of the reduced frequency and eliminate vortex resonance effects as much as possible.

1.2. The Analysis of the Rotational Galloping Behaviour

In the case of a rotational motion of the cross-section, the instantaneous aerodynamic force depends on the (angular) displacement as well as on the (angular) velocity, so that both aerodynamic stiffness and damping effects are present. This is in contrast to translational galloping, as considered by Parkinson & Smith (1964), for which stiffness effects are absent to first order. In our earlier studies, two methods have been developed for the analysis of the dynamic galloping behaviour, both of which are examples of what is known as Melnikov's method for weakly perturbed Hamiltonian (i.e. conservative) systems (Guckenheimer & Holmes 1990). In this method, the stability of the orbits of a Hamiltonian system against the perturbation of a nonlinear forcing is investigated by means of an averaging technique, which effectively determines the average amount of work that is performed by the aerodynamic forces during an oscillation cycle. Stable orbits then provide an approximation of the

limit-cycles of the original nonlinear system. Below, a short characterization of both approaches is given, while for reference the major results will be reviewed in Section 4.

In the *weak-forcing* approach, it is assumed that the wind forces remain sufficiently small, so that the system oscillates in its natural mode (i.e. that which would occur without wind load), and with the amplitude changing only slowly in time. By applying the averaging method the time-rate change of the oscillation amplitude is obtained. The aerodynamic damping can conveniently be expressed in terms of an aerodynamic damping coefficient, that is a function of the amplitude of the oscillation (Haaker & van Der Burgh 1994; van Oudheusden 1995). This provides a description of the build-up or decay in time of the amplitude, for given wind speed and constructional parameters such as the level of the structural damping of the system. Limit cycles are found for those conditions under which the total damping vanishes; galloping curves are obtained by displaying the limit-cycle amplitudes as a function of the wind speed. Note that, in this approach, stiffness effects have been discarded altogether. Detailed experimental results for an oscillator where the system damping is a combination of viscous and frictional damping have been reported for a beam with a square cross-section (van Oudheusden 1996a). Good correspondence was found between the observed galloping amplitudes, and the predictions based on static aerodynamic force measurements. Deviations were only found for large oscillation amplitudes at low wind speeds, where the experimental amplitudes were significantly higher than predicted.

The *strong-forcing* approach is suggested by the observation that for large wind speeds the leading-order aerodynamic effect is of conservative nature, viz., the wind force due to the static displacement alone. A modified analysis is obtained by including this term, in the form of an "aerodynamic potential", in the Hamiltonian of the oscillation (van Oudheusden 1996b; Haaker & van Oudheusden 1997). This Hamiltonian system describes the aerodynamic stiffness effect and reveals how this affects the frequency and mode shape, as a function of wind speed and oscillation amplitude. As a consequence of the nonlinear nature of the aerodynamic forcing, the mode shape is no longer harmonic, while in addition the frequency becomes amplitude-dependent. These predictions showed very good correspondence with the experiments. Also, a (nonharmonic) averaging of the equation of motion provides the stability of the oscillation, revealing typical strong-forcing effects on the galloping behaviour, such as an increase in the limit-cycle amplitude for a given wind speed and the existence of a critical wind speed, above which dynamic divergence of the motion occurs. These aspects were indeed observed in the experiments. The analysis furthermore predicts that the damping coefficient (and hence the stability) is not noticeably affected by the strong-forcing effects, as long as no significant distortion of the mode shape from a harmonic shape occurs. This confirms the notion that shifts in the oscillation frequency are not very relevant for (1-dof) galloping, which explains why the weak-forcing approach yields good results even at moderate forcing levels.

These later experiments, which were performed with a beam of rectangular cross-section, showed very good agreement with the predictions as the aerodynamic stiffness effects were concerned. A lesser correspondence, however, was obtained for the damping effect, as derived from the observed galloping (i.e. limit-cycle) amplitudes. A similar deviation as for the rectangular cross-section was found at low wind speeds, but in addition, significant differences occurred at moderate wind speeds as well. This was surprising, in view of the good agreement that had been obtained under similar conditions with the square cross-section, and considering that no such deviations were found for the stiffness effect.

For this reason a more detailed analysis of both the aerodynamic stiffness and damping effects for this cross-section is undertaken in the present paper. In addition, a simplified prediction of the stiffness effect is made on the basis of the weak-forcing theory. The amplitude decay equation that is obtained with the Melnikov method is identical to what is

found with the standard averaging method or the method of two time scales (Guckenheimer & Holmes 1990). These methods allow the use of a slowly varying phase, that provides a first-order prediction of the oscillation frequency. This will be seen to yield a good estimation of the aerodynamic stiffness effect, that is virtually indistinguishable from the results of the strong-forcing theory as long as the oscillation shape remains approximately harmonic. Furthermore, it reveals that an interesting analogy exists between the aerodynamic damping and stiffness coefficients, in the way they are related to the static force coefficient.

2. OSCILLATOR GEOMETRY AND EXPERIMENTAL SET-UP

2.1. Description of the Oscillator Geometry

The oscillator configuration under investigation is a system with one degree of freedom. In Figure 1 the major dimensions of the configuration are defined in the cross-sectional plane, normal to the rotation axis, while Figure 2 provides a schematic view of the set-up used in the experiments. The structure can rotate around a horizontal hinge line, and contains a prismatic beam (cylinder) that is subjected to a homogeneous cross-flow perpendicular to its axis. The span of the beam is denoted by $b = 0{\cdot}35$ m, and the cross-section has a constant rectangular shape, with the height-to-depth ratio h/d being 0·625 in the present investigation. The depth $d = 40$ mm of the cross-section is measured in the streamwise direction, and the height $h = 25$ mm, in the cross-flow direction.

With the centre of gravity of the mobile structure lying below the hinge line, it operates as a pendulum-type oscillator. In the dynamic analysis of the oscillator, the nonlinearity of the restoring force is commonly neglected, and a constant stiffness is assumed. Hence, the aerodynamic forces on the beam are considered to present the only source of nonlinear effects. Throughout the analysis it is further assumed that both the rotation angle θ, as well as the angle of attack α, remain small in magnitude.

2.2. Details of the Model and Oscillator Set-up

The oscillator structure consists of a rigid frame supported on low-friction knife bearings, allowing a rotational motion about a horizontal axis. With adjustable counterweights the weight of the beam model is balanced, while rigidly-connected vertical pendulum arms

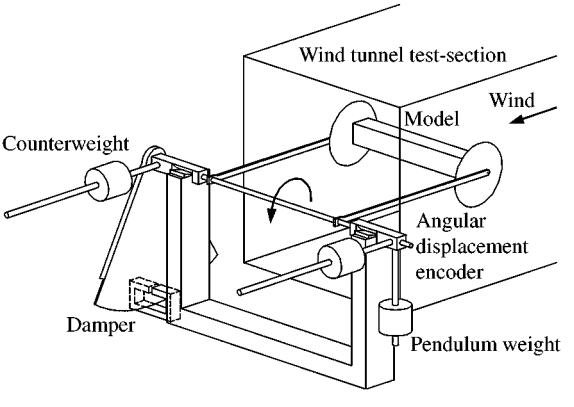

Figure 2. Schematic lay-out of the oscillator; *model*: rectangular beam with circular end plates; *damper*: aluminium inductive damper.

TABLE 1
Oscillator properties

Arm length	$R = 0{\cdot}30$ m
Cylinder span	$b = 0{\cdot}35$ m
Cylinder cross-section	$d \times h = 0{\cdot}040$ m $\times 0{\cdot}025$ m
Natural frequency	$f_0 = 0{\cdot}619$ Hz; $\omega_0 = 3{\cdot}89$ rad/s
Moment of inertia	$I = 0{\cdot}170$ kg m^2
Restoring force stiffness	$k = 2{\cdot}57$ N m
Mass parameter	$\mu = 0{\cdot}00131$

provide the restoring force. The oscillator motion is registered by an optical transducer that is attached to the rotation axis of the structure, with an experimental resolution of about $0{\cdot}1^\circ$.

The major mechanical oscillator properties are summarized in Table 1. The restoring force stiffness was determined from a static calibration, while natural oscillation and damping characteristics were derived from free oscillations and amplitude-decay registrations. Additional damping could be provided by means of an inductive damper. Measurements indicated that the system damping is predominantly of viscous character, but that small amounts of frictional damping and quadratic damping were present as well; a discussion of the damping characterization can be found in Appendix A. Further details of the oscillator construction and the experimental techniques have been documented in van Oudheusden (1998).

The rectangular beam model is equipped with end-plates to obtain a two-dimensional flow over its span and to prevent interference with the boundary layers on the side-walls of the wind tunnel. The wind tunnel is used with an open exit test-section of $0{\cdot}4$ m $\times 0{\cdot}4$ m. By using the oscillator structure as a mechanical balance, the aerodynamic static force data were obtained *in situ*. These are presented in Figure 3 in the form of the aerodynamic coefficient c_M, which will be defined in Section 3. The Reynolds number at which the static data were obtained is about $2{\cdot}7 \times 10^4$, based on the reference velocity U in the test-section and the cross-section depth d. The experimental uncertainty in the value of c_M is approximately 0·02. A tabulated curve-fit representation of the data, as indicated in the figure, has been used for convenience throughout the further analysis. The diagrams in the lower part of Figure 3 give the predicted variation of the corresponding aerodynamic damping and stiffness coefficients, according to the weak-forcing theory, to be discussed in Section 4.2.

The reference flow velocity U, which represents the undisturbed wind speed in the analysis, is measured at the entrance of the test-section, about 1·75 m upstream of the oscillator. Flow blockage evidently increases the effective wind speed which the oscillator experiences locally (the area blockage ratio in the experiment is about 6%). However, as the same reference is used for the reduction of both the static force data and the results of the dynamic tests, the blockage effect is automatically accounted for in the analysis, provided that flow blockage is essentially constant, and not affected by the Reynolds number of the flow or the increased unsteadiness of the flow field during the dynamic tests.

3. QUASI-STEADY MODELLING OF ROTATIONAL GALLOPING

3.1. THE EQUATION OF MOTION

The aerodynamic forces on the structure produce a moment M around the rotation axis of the oscillator. In addition, the motion is affected by system damping which is predominantly

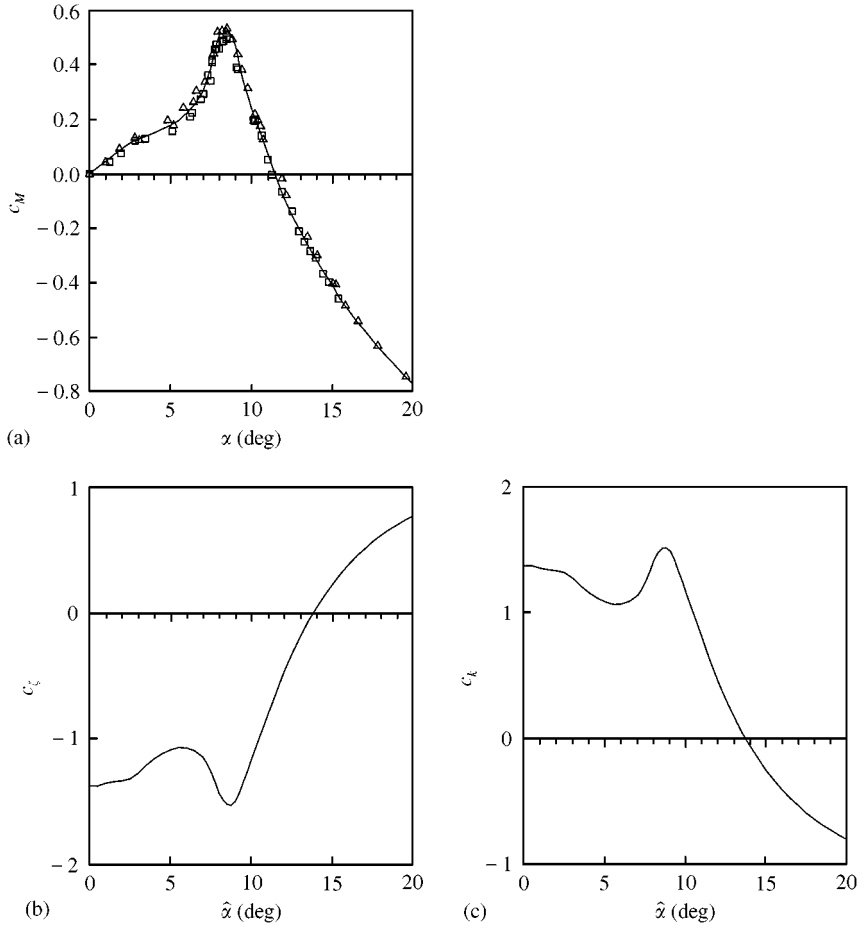

Figure 3. Aerodynamic characteristics of the rectangular cross-section: (a) measured static aerodynamic force characteristics (different symbols indicate data for upwards and downwards displacement, respectively); (b) calculated aerodynamic damping and (c) stiffness coefficients, as function of the aerodynamic amplitude of the oscillation (weak-forcing theory).

of a viscous nature, i.e. with the damping force proportional to the angular velocity. In the following discussion, the effect of the small, nonviscous damping components will be left out of consideration. In the actual data reduction, however, their influence has been included, as has been documented in Appendix A.

The equation of motion in terms of the rotation angle θ of the oscillator is written in dimensionless form, with a dot indicating differentiation with respect to the nondimensional time $\tau = \omega_0 t$, where ω_0 is the natural radial frequency of the system, and reads

$$\ddot{\theta} + \theta = -2\zeta_0\dot{\theta} + \mu u^2 c_M. \tag{1}$$

Here, ζ_0 is the coefficient of the viscous system damping, while the mass ratio μ, the reduced wind speed u and the aerodynamic moment coefficient c_M are defined by

$$\mu = \frac{\rho dbR^3}{2I}, \quad u = \frac{U}{\omega_0 R}, \quad c_M = \frac{2M}{\rho U^2 dbR} \tag{2}$$

with I being the inertial moment of the oscillating structure, ρ the air density and U the wind speed. The relevant dimensions are d for the cross-sectional depth and b for the span of the beam and R for the oscillator arm length (see also Figure 1 and Table 1 for the numerical values).

For the conditions under study, the terms on the right-hand side of equation (1) are typically small, in particular at low wind speeds, resulting in a harmonic oscillator weakly perturbed by system damping and aerodynamic forcing.

3.2. Quasi-Steady Modelling of the Aerodynamic Forces

The aerodynamic moment M around the oscillator hinge axis is dominated by the effect of the normal force F_N on the beam. With h small with respect to R, the effect of the pitching moment around the axis of the beam itself is several orders smaller and can be omitted. Also, the dynamic effects of the beam angular velocity on the aerodynamic forces is neglected, as discussed in van Oudheusden (1995). The coefficient c_M can then be related to the aerodynamic characteristics of the cross-section by

$$c_M = \left(\frac{U_{\text{rel}}}{U}\right)^2 c_N(\alpha). \tag{3}$$

Invoking the quasi-steady flow approach, the normal force coefficient c_N can be derived from wind tunnel data for the configuration under a static rotational displacement. The effective angle of attack α and the relative flow speed U_{rel} are formed from the vectorial difference between the wind speed U and body velocity $U_{\text{rot}} = R\ \mathrm{d}\theta/\mathrm{d}t$, and follow from Figure 1 as

$$\alpha \approx \theta - \frac{\dot{\theta}}{u}, \tag{4}$$

$$\frac{U_{\text{rel}}}{U} = \frac{\cos\theta}{\cos\alpha} \approx 1\,, \tag{5}$$

where the approximation involves the assumption of small angles α and θ. As remarked elsewhere (Haaker & van Der Burgh 1994; van Oudheusden 1995), the resulting system of equations reveal that, for small displacements, the present oscillator is equivalent to a vertically translating prismatic bar, such as considered extensively in Parkinson and Smith (1964) and Parkinson (1989), which simultaneously performs an additional rotation around its axis. This makes the configuration mathematically equivalent to the case of pure torsional galloping (Modi & Slater 1974; Blevins 1990), where a similar dependence on both angular displacement and velocity is found. In the present configuration, however, the quasi-steady approach can be applied with more validity than for torsional motion where it is highly questionable (Nakamura & Mizota 1975; van Oudheusden 1995).

Assuming the oscillator performs a harmonic oscillation at the undamped frequency ω_0 and with a constant amplitude, it follows from equation (4) that the angle of incidence α varies harmonically as well, but with a shift in phase,

$$\theta = \hat{\theta}\sin\tau, \qquad \alpha = \hat{\alpha}\sin(\tau - \phi). \tag{6}$$

Here, the hatted variables are used to denote the amplitude of a time-periodic quantity. For convenience, we may call $\hat{\theta}$ the *structural* amplitude and $\hat{\alpha}$ the *aerodynamic* amplitude of the oscillation. From equations (4) and (6), we derive

$$\hat{\alpha} = \hat{\theta}\sqrt{1 + \frac{1}{u^2}}, \qquad \tan\phi = \frac{1}{u}. \tag{7}$$

Note that the kinematics of the oscillation is governed only by the value of the reduced wind speed u, and that the phase lag ϕ is independent of the oscillation amplitude. For the limiting situations, where u is either much smaller or larger than unity, the above expressions reveal that, for $u \ll 1$ the configuration is aerodynamically equivalent to a purely translational motion, with α dominated by the velocity component of the motion. On the other hand, for $u \gg 1$, the oscillator can be regarded to operate in a "full rotation regime", with α nearly equal to the rotation angle θ itself. Note, however, that although the phase lag is seen to decrease as u grows, its existence remains essential for the motion to be able to extract energy from the flow field (van Oudheusden 1995).

Considering now the more general situation, where the oscillation is harmonic but at an arbitrary frequency, i.e. not necessarily identical to ω_0, so that $\theta = \hat{\theta} \sin \Omega\tau$, where $\Omega = \omega/\omega_0$ is the frequency ratio. Then, again starting from equation (4), the following relations are obtained which relate structural motion and aerodynamic behaviour:

$$\hat{\alpha} = \hat{\theta} \sqrt{1 + \frac{\Omega^2}{u^2}}, \qquad \theta = \frac{\hat{\theta}^2}{\hat{\alpha}^2}\left(\alpha + \frac{\dot{\alpha}}{u}\right), \qquad \dot{\theta} = \frac{\hat{\theta}^2}{\hat{\alpha}^2}\left(\dot{\alpha} - \Omega^2 \frac{\alpha}{u}\right). \tag{8}$$

4. ANALYSIS OF THE DYNAMIC BEHAVIOUR

4.1. Linear Analysis

To illustrate the stiffening and dampening effects of the aerodynamic forcing, the first situation to be considered is where c_M is linear in α, say

$$c_M = a\alpha, \tag{9}$$

where a is a constant. For a symmetric cross-section, this can be regarded as a linearization around the equilibrium position. Substitution of this expression into the equation of motion, equation (1), and with α given by equation (4), yields

$$\ddot{\theta} + \theta = -2\zeta_0\dot{\theta} + \mu u a(u\theta - \dot{\theta}). \tag{10}$$

This reveals that the effect of the aerodynamic forces can be interpreted as the sum of an aerodynamic stiffness and an aerodynamic damping. The solution can be written as $\theta(\tau) = \hat{\theta}(\tau)\cos(\Omega\tau)$, and which displays the following properties:

$$\frac{\mathrm{d}\hat{\theta}}{\mathrm{d}\tau} = -\zeta_0\hat{\theta} - \mu u \frac{a}{2}\hat{\theta}, \qquad \Omega = \frac{\omega}{\omega_0} = \sqrt{1 - \mu u^2 a}. \tag{11}$$

The damping and stiffness effect have been expressed here in terms of, respectively, the amplitude decay rate $\mathrm{d}\hat{\theta}/\mathrm{d}\tau$, and the frequency ratio Ω, where the effect of the damping on the frequency has been neglected. Note that the aerodynamic damping effect is proportional to u, and the aerodynamic stiffness effect to u^2. Also, when a is negative the aerodynamic force is destabilizing in the dynamic sense (negative damping), which corresponds to Den Hartog's stability criterion (Blevins 1990), but statically stabilizing (positive stiffness) for the present oscillator configuration.

4.2. Weak-Forcing Galloping Analysis (Low Wind Speeds)

Under weak-forcing conditions, the nonlinear system of equation (1) can be regarded as a perturbation of the free motion of the undamped oscillator. Using the general method of two time scales, the solution is written as

$$\theta = \hat{\theta}\sin(\tau + \psi), \qquad \dot{\theta} = \hat{\theta}\cos(\tau + \psi). \tag{12}$$

Applying standard averaging techniques, the following equations are obtained for the slow time behaviour of the amplitude $\hat{\theta}$ and phase angle ψ:

$$\frac{\mathrm{d}\hat{\theta}}{\mathrm{d}\tau} = -\zeta_0\hat{\theta} - \mu u c_\zeta \hat{\theta}, \tag{13}$$

$$\frac{\mathrm{d}\psi}{\mathrm{d}\tau} = \mu u^2 c_k, \tag{14}$$

where c_ζ and c_k are aerodynamic damping and stiffness coefficients, conveniently defined as more or less the generalization of the linear results of equation (11), and which follow from the averaging procedure as

$$c_\zeta = -\frac{u}{\hat{\theta}^2}\langle c_M(\alpha)\dot{\theta}\rangle, \qquad c_k = -\frac{1}{\hat{\theta}^2}\langle c_M(\alpha)\theta\rangle. \tag{15}$$

Here the brackets $\langle\ \rangle$ indicate the averaging operation, which is performed over an oscillation period, during which the slowly varying amplitude and phase are assumed constant. Using relations (8) with $\Omega = 1$, these coefficients can be expressed completely in terms of α, yielding

$$c_\zeta = \frac{\langle c_M(\alpha)(\alpha - u\dot{\alpha})\rangle}{\hat{\alpha}^2} = \frac{\langle c_M(\alpha)\alpha\rangle}{\hat{\alpha}^2}, \tag{16}$$

$$c_k = -\frac{\langle c_M(\alpha)(\alpha + \dot{\alpha}/u)\rangle}{\hat{\alpha}^2} = -\frac{\langle c_M(\alpha)\alpha\rangle}{\hat{\alpha}^2}. \tag{17}$$

In both expressions, the second term vanishes upon averaging, for any function $c_M(\alpha)$. For the damping coefficient, this second term represents the conservative component of the aerodynamic force, while for the stiffness coefficient, it is the dissipative component.

This reveals that both c_ζ and c_k are functions only of $\hat{\alpha}$, the aerodynamic amplitude of the oscillation. Moreover, the way they are related to $\hat{\alpha}$ through the steady force coefficient c_M is identical for both coefficients, to the extent that $c_\zeta = -c_k$. Note that the result that was obtained in Section 4.1 for a linear forcing, $c_\zeta = -c_k = a/2$, is seen to constitute a specific case of this relation. Figure 3(b,c) displays the predicted $c_\zeta(\hat{\alpha})$ and $c_k(\hat{\alpha})$ functions, for the experimental configuration under consideration, and derived from the measured static $c_M(\alpha)$ curve.

The damping coefficient c_ζ describes the stability of the motion, as reflected by the amplitude-transient relation of equation (13). Similarly, the aerodynamic effect on the oscillation frequency ratio $\Omega = \omega/\omega_0$ is governed by the stiffness coefficient c_k, according to

$$\Omega = \frac{\omega}{\omega_0} = 1 + \frac{\mathrm{d}\psi}{\mathrm{d}\tau} = 1 + \mu u^2 c_k. \tag{18}$$

In the sense of a first-order approximation for small values of μu^2, the following expression may be regarded to be equivalent to equation (18):

$$\Omega = \sqrt{1 + 2\mu u^2 c_k}. \tag{19}$$

This second form is preferred for practical predictions, because it is expected to yield a better description of stronger forcing effects, as motivated by comparison with equation (11), which is the exact result for the linear forcing case.

Note, furthermore, the interesting observation that at the amplitude where the aerodynamic damping is zero, the aerodynamic stiffness effect vanishes as well. As a consequence,

for cases where the aerodynamic damping is dominant, the limit-cycle oscillation is predicted to occur at approximately the natural frequency, even at wind speeds where the aerodynamic forcing levels have become significant.

4.2.1. *Effect of oscillation frequency*

According to the weak-forcing approach the aerodynamic stiffness has to first order no effect on the stability of the oscillation. It can be shown that this is true even when significant variations of the frequency occur, provided that the oscillation shape remains approximately harmonic. This can be illustrated by the following analysis, in which the equation of motion is adapted by including the frequency ratio $\Omega = \omega/\omega_0$ in the stiffness term, to represent a change in the natural frequency,

$$\ddot{\theta} + \Omega^2\theta = -2\zeta_0\dot{\theta} + \mu u^2 c_M(\alpha). \tag{20}$$

The definition of the nondimensional time $\tau = \omega_0 t$ remains unaltered, but with ω_0 now merely acting as a reference scale, without necessarily having the meaning of the natural frequency. Application of the averaging method is now to be carried out using

$$\theta = \hat{\theta}\sin(\Omega\tau), \qquad \dot{\theta} = \hat{\theta}\Omega\cos(\Omega\tau), \tag{21}$$

which yields the following amplitude-transient equation:

$$\frac{\mathrm{d}\hat{\theta}}{\mathrm{d}\tau} = -\zeta_0\hat{\theta} - \mu u c_\zeta \hat{\theta}. \tag{22}$$

The result for c_ζ as function of $\hat{\alpha}$ is found to remain unaffected, as follows from

$$c_\zeta = -\frac{u}{\Omega^2\hat{\theta}^2}\langle c_M(\alpha)\dot{\theta}\rangle = \frac{\langle c_M(\alpha)(\Omega^2\alpha - u\dot{\alpha})\rangle}{\Omega^2\hat{\alpha}^2} = \frac{\langle c_M(\alpha)\alpha\rangle}{\hat{\alpha}^2}, \tag{23}$$

whereas with $\Omega^2 = 1 + \mathrm{O}(\mu u^2)$, the effect of Ω on the $\hat{\alpha}$–$\hat{\theta}$ relation, see equation (8), is only $\mathrm{O}(\mu)$ and therefore negligible, as in the present experiments the value of μ lies in the order of 10^{-3}. It can hence be concluded that a shift in the oscillation frequency has no notable effect on the stability behaviour, provided that μ is small (and that the nonviscous damping effects are not dominant, see Appendix A).

4.3. Strong-Forcing Galloping Analysis (High Wind Speeds)

As outlined above, the aerodynamic forcing contains an aerodynamic stiffness effect. This may become appreciable with respect to the elastic forces, for increased values of the parameter $\varepsilon = \mu u^2$, which describes the strength of the 'perturbation level' of the mechanical oscillator system by the aerodynamic forces. The mass parameter μ is generally small when considering a structure in a wind field. Therefore, also in the present context ε can only become significant when increasingly high wind speeds are considered. Furthermore, note from equations (11) and (14), that the aerodynamic stiffness effect is quadratic in u, whereas the damping contribution is linear in u. It is generally true, for large u, which is a necessary condition for stiffness effects to become relevant, that the leading order term of the aerodynamic forcing leads to a conservative contribution to the energy balance of the oscillation, while the largest dissipative term is one order of u smaller than this, as illustrated by the following Taylor expansion:

$$\mu u^2 c_M(\alpha) = \mu u^2 c_M\left(\theta - \frac{\dot{\theta}}{u}\right) \approx \mu u^2 c_M(\theta) - \mu u c_{M_\alpha}(\theta)\,\dot{\theta} \tag{24}$$

with c_{M_α} indicating the local slope of the $c_M(\alpha)$ curve. This observation provides a way to extend the perturbation analysis to higher wind speeds, by considering the Hamiltonian system that is obtained by including the (leading-order) aerodynamic stiffness terms, to which the remaining nonconservative terms can be regarded to act as a weak perturbation, i.e. writing the equation of motion as

$$\frac{\mathrm{d}}{\mathrm{d}\tau} H_s(\theta, \dot{\theta}) = F_s(\theta, \dot{\theta}), \tag{25}$$

where H_s is the effective Hamiltonian for the strong-forcing analysis,

$$H_s(\theta, \dot{\theta}) = \frac{\dot{\theta}^2 + \theta^2}{2} + \varepsilon c_G(\theta), \tag{26}$$

and F_s is the perturbing forcing function,

$$F_s(\theta, \dot{\theta}) = -2\zeta_0 \dot{\theta}^2 + \varepsilon(c_M(\alpha) - c_M(\theta))\,\dot{\theta}. \tag{27}$$

In equation (26), c_G is defined from $c_M(\theta) = -\mathrm{d}c_G(\theta)/\mathrm{d}\theta$ and is the coefficient of what can be regarded the mechanical potential of the oscillator due to the steady aerodynamic force that results from a static displacement angle θ (an "aerodynamic potential"). This approach relaxes the condition of validity of the perturbation analysis to $u \ll \mu^{-1}$, instead of $u \ll \mu^{-1/2}$ which applies in the weak-forcing theory, and which for the present value of μ extends the condition from $u \ll 30$ to $u \ll 10^3$. A more rigorous mathematical treatment of the method can be found in Haaker & van Oudheusden (1997).

The oscillation shape is approximated by the orbits (periodic solutions) of the Hamiltonian system, that are generated by constant values of H_s. Assuming the aerodynamic force function c_M is antisymmetric in α (as it is for a symmetric cross-section), the amplitude $\hat{\theta}$ of the oscillation can be defined uniquely, as the extreme positions of an orbit are located symmetrically with respect to $\theta = 0$. The constant value of the Hamiltonian of the orbit can be related to the oscillation amplitude, $\hat{\theta}$, as

$$H_s(\theta, \dot{\theta}) = H_s(\hat{\theta}, 0) = \frac{\hat{\theta}^2}{2} + \varepsilon c_G(\hat{\theta}). \tag{28}$$

Further, the orbits possess symmetry with respect to both axes of the $(\theta, \dot{\theta})$-phase plane,

$$\dot{\theta}^2 = \hat{\theta}^2 - \theta^2 + 2\varepsilon[c_G(\hat{\theta}) - c_G(\theta)] \tag{29}$$

with which the oscillation frequency is obtained as

$$\Omega = \left(\frac{2}{\pi} \int_0^{\hat{\theta}} \frac{\mathrm{d}\theta}{\dot{\theta}}\right)^{-1} = \left(\frac{2}{\pi} \int_0^{\hat{\theta}} [\hat{\theta}^2 - \theta^2 + 2\varepsilon\{c_G(\hat{\theta}) - c_G(\theta)\}]^{-1/2}\,\mathrm{d}\theta\right)^{-1}. \tag{30}$$

To summarize the major conclusions of the strong-forcing analysis as far as the mode shape is concerned, the aerodynamic stiffness effects result in a change of the oscillation frequency, where due to the nonlinearity of the aerodynamic stiffness, the frequency has become amplitude dependent. Also, the oscillation shape is distorted from its original harmonic shape. For the present configuration, where the aerodynamic force is statically stabilizing for small deflections, but statically destabilizing at larger angles, the oscillation frequency decreases for larger amplitudes, up to the point where divergence of the motion is found to occur.

The stability of the oscillation is obtained from averaging equation (25), which with equations (27) and (29), yields

$$\frac{\mathrm{d}}{\mathrm{d}\tau} H_s(\theta, \dot{\theta}) = -(\zeta_0 + \mu u c_\zeta)\langle 2\dot{\theta}^2 \rangle, \tag{31}$$

while equation (28) allows the left-hand side to be related to the amplitude decay, $\mathrm{d}\hat{\theta}/\mathrm{d}\tau$, by

$$\frac{\mathrm{d}}{\mathrm{d}\tau} H_s(\theta, \dot{\theta}) = \frac{\mathrm{d}}{\mathrm{d}\hat{\theta}} H_s(\hat{\theta}, 0) \frac{\mathrm{d}\hat{\theta}}{\mathrm{d}\tau} = [\hat{\theta} - \varepsilon c_M(\hat{\theta})] \frac{\mathrm{d}\hat{\theta}}{\mathrm{d}\tau}. \tag{32}$$

The aerodynamic damping coefficient, c_ζ, defined in a similar manner as in the weak-forcing approach, now follows as

$$c_\zeta = -u \frac{\langle (c_M(\alpha) - c_M(\theta))\dot{\theta} \rangle}{\langle 2\dot{\theta}^2 \rangle} = -u \frac{\langle c_M(\alpha)\dot{\theta} \rangle}{\langle 2\dot{\theta}^2 \rangle}. \tag{33}$$

Alternatively, with the approximation for $u \gg 1$ and invoking equation (24), c_ζ can be written as

$$c_\zeta \approx \frac{\langle c_{M_s}(\theta)\dot{\theta}^2 \rangle}{\langle 2\dot{\theta}^2 \rangle}. \tag{34}$$

This shows that, in general but provided that u is large, c_ζ is therefore a function of the oscillation amplitude $\hat{\theta}$ and, through equation (29), of the perturbation parameter ε as well.

Determination of the aerodynamic stiffness and damping effects for a given aerodynamic characteristic $c_M(\alpha)$, requires numerical evaluation of the integral in equation (30) to determine the frequency, and of the averaged expressions in equations (31) and (33) or (34) in order to assess the stability of the oscillation. The value of the aerodynamic stiffness coefficient c_k can be inferred from Ω, by regarding equation (19) as its general definition. As will be shown later, it is found that the differences with the weak-forcing theory are very small even for significant variations of the frequency, as long as the oscillation shape remains approximately harmonic. This is in accordance with what was found in Section 4.2 by means of the simplified aerodynamic stiffness analysis based on equation (20).

Finally, a remark should be made on the behaviour of the strong-forcing theory in the limit of small ε. For a proper asymptotic behaviour the results should then evidently become identical to those of the weak-forcing theory. Indeed, for a harmonic oscillation at the natural frequency ω_0, the expression of equation (33) for the aerodynamic damping coefficient reduces directly to equation (15). Similarly, partial integration allows the expression of equation (34) to be reduced to the form of equation (16). The only difference between these latter results, however, lies in the fact that for the weak-forcing theory c_ζ is a function of $\hat{\alpha}$, whereas in the strong forcing $\hat{\theta}$ is used. There is no direct disagreement in this, as the derivation of equation (34) was based on equation (24) which is valid only for $u \gg 1$, in which case $\hat{\theta} \approx \hat{\alpha}$. This observation suggests that, for a proper comparison between weak- and strong-forcing predictions, the oscillation amplitude is to be interpreted in the aerodynamic sense (i.e. taking $\hat{\alpha}$) also in the strong-forcing approach. A similar argument holds for the aerodynamic stiffness coefficient, but at low wind speeds this effect is evidently of less practical relevance for the dynamic behaviour anyway.

5. EXPERIMENTAL INVESTIGATION

5.1. Galloping Curves

Dynamic measurements were carried out in the form of galloping tests, where the evolution of the oscillation amplitude in time was recorded, and during which the wind speed and the

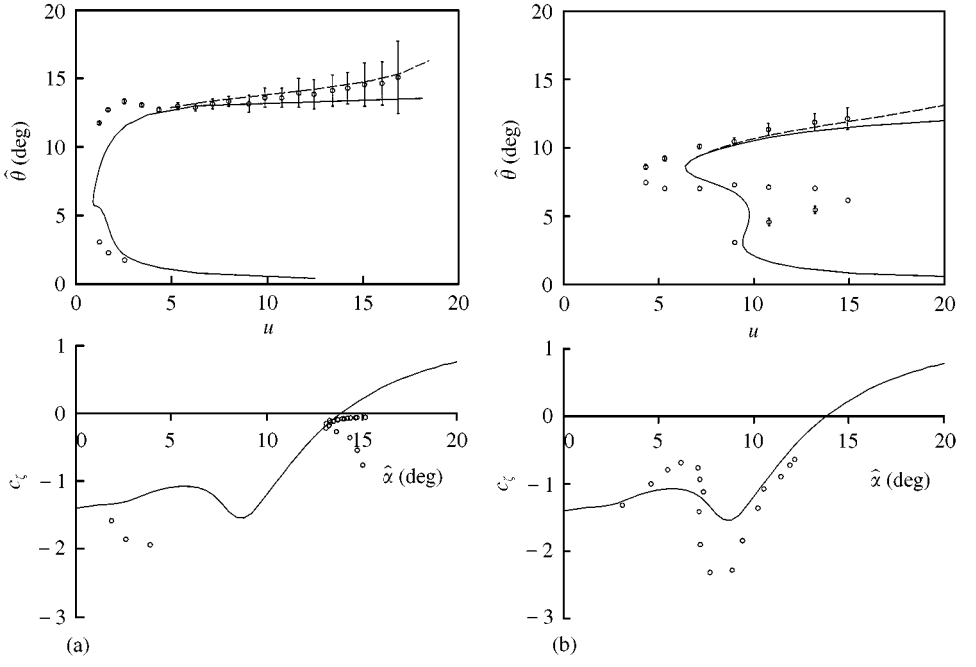

Figure 4. Galloping amplitudes for different damping levels. Symbols indicate experiments and curves quasi-steady predictions (——, weak-forcing theory; – – –, strong-forcing theory). (a) damper setting "0"; (b) damper setting "4".

system damping were maintained at a constant level. Limit-cycle amplitudes were identified and in order to investigate the possible presence of multiple limit cycles, tests were performed with different initial amplitudes of the oscillation. Examples of such test results have been reported in van Oudheusden (1996a,b). This procedure was then repeated for a large number of different wind speeds to obtain the galloping curve, i.e. the dependence of limit cycle amplitudes on wind speed. Galloping tests were conducted for five different levels of the system damping. In the context of the present discussion, only the galloping curves for the lowest and highest damping levels are presented in some detail, in Figure 4. The values of the corresponding damping parameters can be found in Appendix A.

The galloping curve for the lower damping case is shown in Figure 4(a), where the data symbols display the observed limit-cycle amplitudes, $\hat{\theta}$, as a function of the reduced wind speed u. Note that, at low wind speeds, some data were obtained near the lower branch of unstable limit cycles as well. The solid and dashed curves represent the predictions according to, respectively, the weak- and strong-forcing theories. These differ only in an additional increase of the limit cycle amplitude with u for higher wind speeds, and which appears fairly consistent with the experiments. For the stable limit cycles, the error bar indicates the range of unsteady variation of the limit cycle amplitude in the experiments, which grows with wind speed due to the increased strength of the unsteady component of the aerodynamic forces. Notwithstanding this unsteadiness, the strong-forcing theory appears to provide a good prediction of the mean amplitude value and its increase with wind speed. Deviations from the (quasi-steady) theory occur in particular at low wind speeds, for u below the value of 5, where the large limit-cycle amplitudes lie significantly higher than predicted. Similar behaviour has been observed for the rotational galloping of a square cross-section (van Oudheusden 1996a).

A further investigation of the validity of the quasi-steady analysis can be carried out by using the observed limit cycle amplitudes to calculate the corresponding values of the aerodynamic damping coefficient c_ζ, where, according to equation (13),

$$c_\zeta = -\frac{\zeta_0}{\mu u}. \tag{35}$$

In the bottom diagram of Figure 4(a), these experimental results are compared with the quasi-steady prediction according to the weak-forcing theory, and which employs the static force measurements. As suggested by the theory, $\hat{\alpha}$ is used as the relevant amplitude along the horizontal axis, and which is calculated from equation (7). Also this representation of the data reveals that there are significant deviations between experiment and theory. This holds especially for the data that correspond to the low wind speed range, and with the discrepancy increasing for progressively lower wind speeds. The data points that lie close to the horizontal axis represents the increase of the galloping amplitude due to the strong wind effects. The galloping curve for this configuration contains information mainly for large oscillation amplitudes. Some data have been obtained for small amplitudes, but as these are derived from unstable limit-cycle amplitudes they may be not very accurate.

In Figure 4(b) the galloping curve is depicted for the highest damping case considered in the experiments. The experimentally observed region which displays multiple limit cycles, is seen to extend to a much larger range of wind speeds than predicted. This is also reflected in the lower graph, which shows that a much larger variation of the damping coefficient with amplitude occurs, than is predicted on the basis of the steady force characteristics.

For evidence to be discussed later, it is unlikely that this effect can be attributed to errors in the static force measurements, which would moreover have to be quite large in order to explain the extent of the differences observed here. The most likely explanation is, hence, deviations from the assumptions on which the quasi-steady predictions are based.

5.2. Stiffness and Damping Curves at Constant Wind Speed

It should be realized that, although the set of damping data in Figure 4(b) provide a more or less continuous curve in the c_ζ-graph, they represent conditions at largely varying values of u, and it is only on the basis of the quasi-steady theory that a unique curve is expected to occur. However, the experiments, Figure 4(a) in particular, suggest that there is evidence of a significant dependence of the damping curve on wind speed. In order to investigate this in more detail, the variation of the stiffness and damping with amplitude needs to be studied for fixed values of the reduced wind speed u.

The limit-cycle amplitudes of a single galloping curve contain only very limited information about the damping behaviour at a given wind speed. This can be supplemented by generating different galloping curves, by varying the system damping level. In the present investigation, five damping levels were applied (see Appendix A for details). In addition to these data derived from limit-cycle oscillations, a second procedure was followed in which an analysis was made of recordings of the transient oscillation behaviour. To this end, an accurate registration of the motion was performed for a limited number of test runs. These time records of the oscillator displacement were subsequently analyzed to obtain detailed aerodynamic stiffness and damping characteristics as a function of the oscillation amplitude, at constant wind speed. This was achieved by determining the instantaneous values of the amplitude and frequency of the oscillation, after which the amplitude decay or amplification rate was derived, using data of five adjoining semi-periods. In this way a more or less continuous damping and stiffness curve over a range of amplitudes for a fixed value of u can

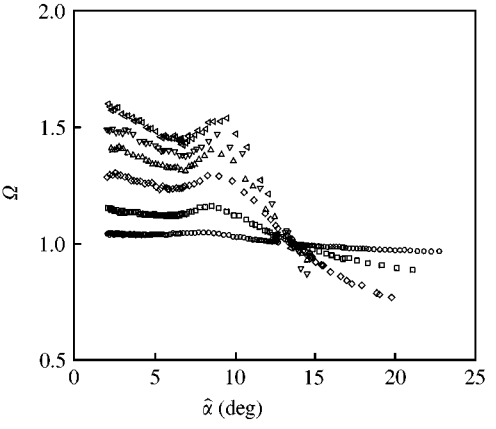

Figure 5. Frequency–amplitude characteristics at different wind speeds; ○ $u = 4{\cdot}4$, $\varepsilon = 0{\cdot}025$; □ $u = 9{\cdot}1$, $\varepsilon = 0{\cdot}108$; ◇ $u = 13{\cdot}4$, $\varepsilon = 0{\cdot}236$; △ $u = 16{\cdot}0$, $\varepsilon = 0{\cdot}337$; ▽ $u = 17{\cdot}7$, $\varepsilon = 0{\cdot}409$; ◁ $u = 19{\cdot}4$, $\varepsilon = 0{\cdot}491$.

be obtained from a single time record. The experimental inaccuracy is about 0.1° in the amplitude, and less than 1% in the frequency ratio Ω, for amplitudes above 1–2°.

In Figure 5 the frequency ratio Ω is shown for a number of different wind speeds and is plotted as a function of the aerodynamic amplitude of the oscillation, $\hat{\alpha}$, as suggested by the quasi-steady theory. In correspondence with theory, the amplitude for which the stiffness effect vanishes is indeed found to be approximately the same for all wind speeds. Its value, about 13.5°, agrees well with the predictions (cf. Figure 3).

From the values of the frequency ratio Ω and the decay rate $\mathrm{d}\hat{\theta}/\mathrm{d}\tau$ obtained from the time-record data, corresponding values of the aerodynamic stiffness and damping coefficients can be calculated, according to equations (19) and (22), as

$$c_k = \frac{\Omega^2 - 1}{2\mu u^2}, \qquad c_\zeta = -\frac{1}{\mu u}\left(\frac{1}{\hat{\theta}}\frac{\mathrm{d}\hat{\theta}}{\mathrm{d}\tau} + \zeta_0\right). \tag{36}$$

Note that, for very low values of $\varepsilon = \mu u^2$, which occur at low wind speeds, Ω is very nearly unity, so that the determination of the stiffness effect becomes unreliable, while under these conditions, the small effect of the nonlinearity of the pendulum-type restoring force needs to be taken into account as well. Furthermore, as is discussed in Appendix A, the value of Ω is involved also in the calculation of the damping coefficient, when the nonviscous components of the damping are included.

For the predominant part of the galloping investigation, a reduced data-storage procedure had been followed, in which only the subsequent extreme positions of the oscillator motion were recorded. These data records therefore provide only sequential amplitude data, but contain no accurate time data from which the frequency can be determined. Also from these records the damping curves were derived, by the same method as above; for this the missing frequency data is provided for by an estimation using the weak-forcing theory. As analysis of the frequency data from the complete records reveals, this prediction is in close agreement with experiments for those conditions where the stiffness effects are relevant. The same frequency estimate was also used in the calculation of the damping data from the limit-cycle amplitudes.

For increasing values of the reduced wind speed, Figures 6 and 7 depict, respectively, the values of the aerodynamic damping and stiffness coefficients, plotted against $\hat{\alpha}$. The data

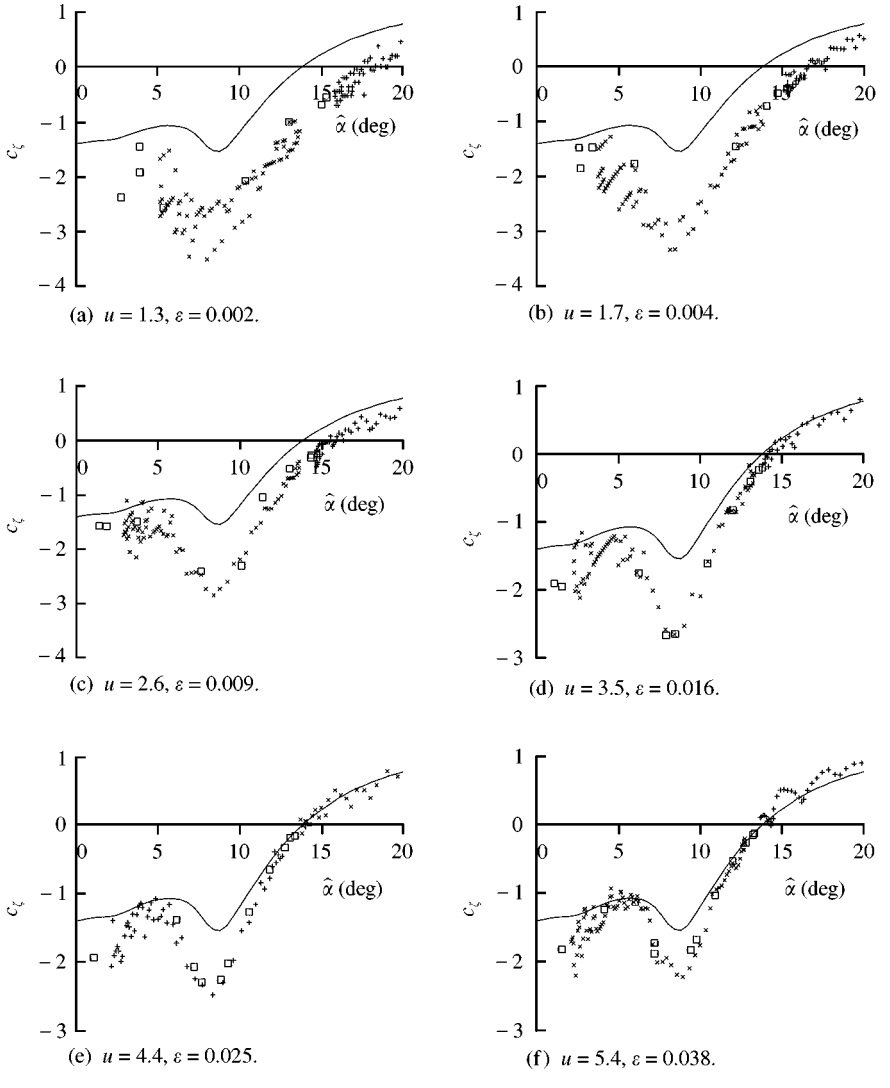

Figure 6. Aerodynamic damping coefficients. Symbols indicate data derived from time records (+ and ×) or from limit-cycle amplitudes (□); ——, weak-forcing theory; – – –, strong-forcing theory.

that are derived from the transient records are represented by the small symbols (such as + and ×), where different symbols indicate different individual runs (time records). The damping data derived from the limit-cycle amplitudes in the galloping curves are denoted by the box symbols (□). In general, there is good agreement between the results of the two approaches. Especially at low wind speeds, the transient data show a fair amount of scatter, because the amplitude change over an oscillation period is only very small, so that it is difficult to determine the local amplitude decay or amplification rate accurately. For the highest wind speed, on the other hand, there is some disagreement between the limit-cycle data and the transient data at large amplitudes. In this respect it is to be noted that the time-record data correspond to a particular realization of a transient oscillation motion. The increased flow unsteadiness at higher wind speeds, as witnessed also by the error bars in Figure 4, is likely to affect the accuracy of the time-record analysis, while also larger

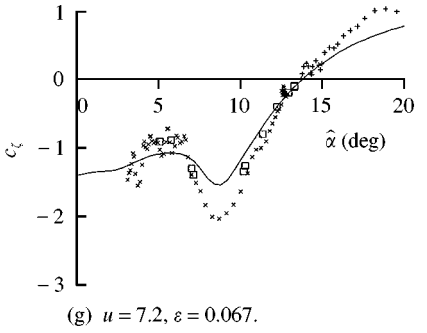

(g) $u = 7.2$, $\varepsilon = 0.067$.

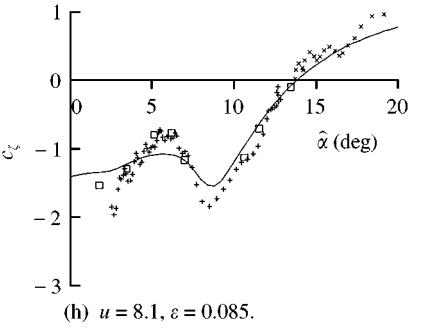

(h) $u = 8.1$, $\varepsilon = 0.085$.

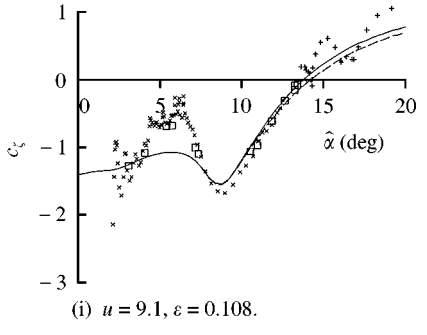

(i) $u = 9.1$, $\varepsilon = 0.108$.

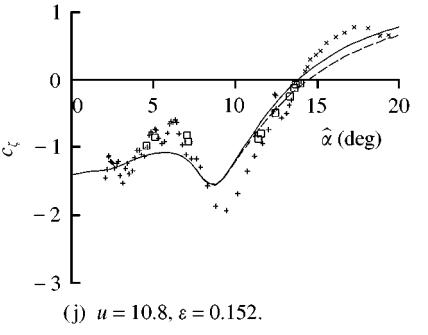

(j) $u = 10.8$, $\varepsilon = 0.152$.

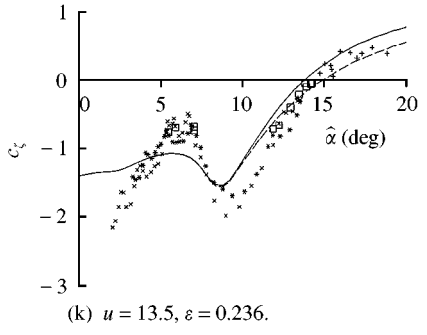

(k) $u = 13.5$, $\varepsilon = 0.236$.

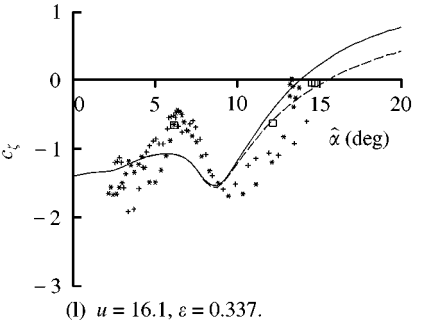

(l) $u = 16.1$, $\varepsilon = 0.337$.

Figure 6. *Continued.*

variations may occur among different realizations. The galloping data, on the other hand, are based on the average values of the limit-cycle amplitudes, and are more representative of the average damping effect under these conditions. The latter also show good agreement with the theory.

The different curves represent the quasi-steady predictions, with the solid and dashed lines indicating, respectively, the weak- and strong-forcing theory; the latter is included only when $\varepsilon > 0.1$. Significant nonlinear stiffness effects are seen to occur only at large amplitudes and high wind speeds, otherwise the differences between the two predictions are very small.

At moderate and high wind speeds the stiffness effect is very well predicted, which may confirm the correctness of the static force measurements, and their relative insensitivity to Reynolds number. The agreement for the damping effect, however, is much less. In particular, for the intermediate amplitude range the variation with the amplitude is larger

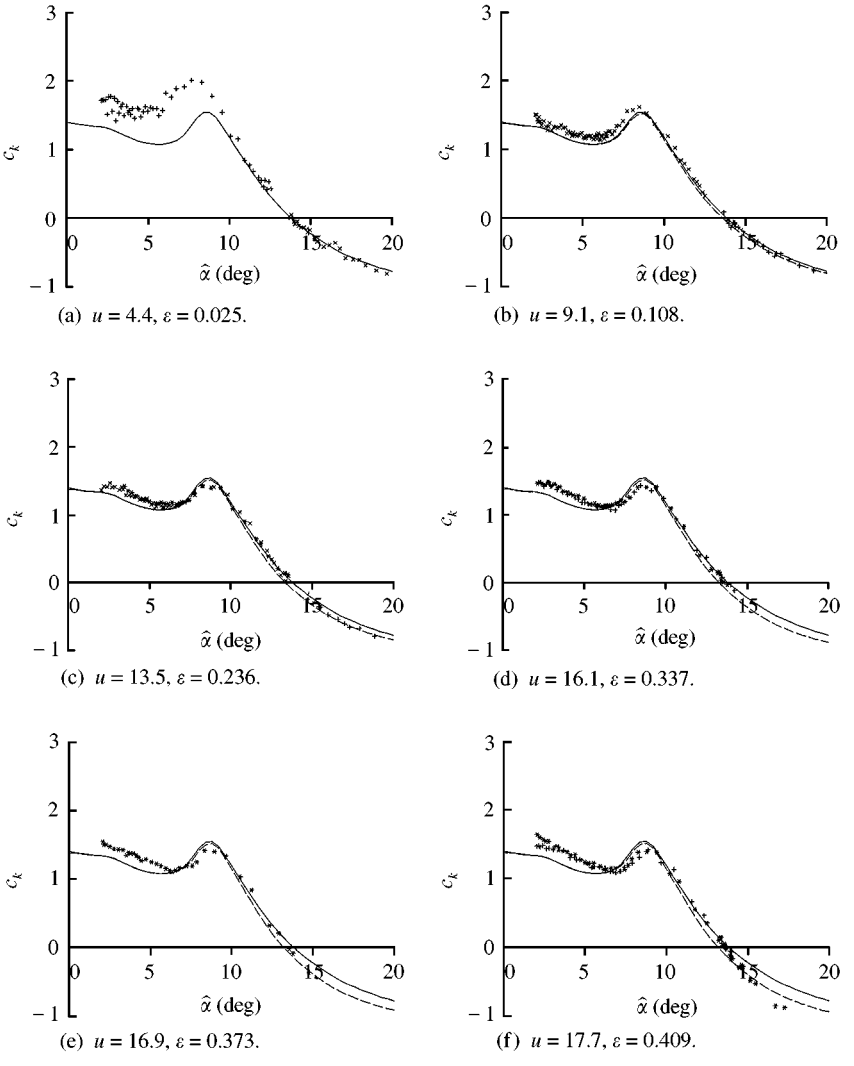

Figure 7. Aerodynamic stiffness coefficients. Symbols and line types are the same as in Figure 6.

than predicted. At decreased wind speeds additional effects are seen to occur. At $u = 4{\cdot}4$, both stiffness and damping effects are seen to be significantly increased with respect to the predictions, for amplitudes up to 10°, whereas for higher amplitudes, correspondence with theory is again good. When progressively lowering the wind speed, the damping effect is seen to be increased further (no reliable stiffness data could be extracted for these conditions). In addition, the intersection with the horizontal axis, representing the amplitude for which the damping vanishes, is observed to move to higher values. This latter effect explains why the galloping curve of Figure 4(a) displays increased values of the galloping amplitude at low wind speeds. Also, from these results it becomes clear that the variation observed in the damping curve of Figure 4(b) has been amplified by this velocity dependence: the relatively weak damping data (near 6–7°) correspond to limit-cycle oscillations at high wind speeds, whereas the strong damping data (near 8–9°) correspond to low wind speeds.

6. DISCUSSION

6.1. The Aerodynamics of Galloping

In summary, the results of Figures 6 and 7 reveal that for moderate wind speeds the correspondence between experiments and theory is very good where the stiffness effects are concerned, whereas for the damping effect, significant deviations are observed. This is remarkable, as fairly good agreement for the damping predictions had been found in similar experiments with a square cross-section. The quasi-steady theory predicts both effects to be identical, albeit opposite in sign, so the good agreement for the stiffness data would rule out significant and systematic errors in the static force data. Additional deviations from theory were observed to occur at low wind speeds, with the value of the reduced wind speed u below 5, which had also been found for the square section. This may suggest that the latter effect is possibly to be attributed to a common cause, such as a Reynolds number effect in the set-up or a fundamental shortcoming of the quasi-steady approach, whereas the first effect may be more specific to the rectangular cross-section.

In this section, a number of effects are considered as possible or likely causes for the observed deviations. At present, insufficient experimental evidence is available to support a definitive explanation. This would certainly require additional experimental validation or, alternatively, a numerical investigation of suggested trends. For these reasons the discussion is necessarily restricted to a tentative assessment of whether certain effects can be held responsible for these deviations and, if so, in what sense and to which extent.

For reference and better understanding, let us first review the characteristics of the separated flow that occurs around rectangular cross-sections, and associated with it the mechanisms of the galloping instability behaviour. The basic flow structure of these shapes and the way this affects galloping have been discussed in detail by several authors, see, e.g. Nakamura & Hirata (1989, 1994), Novak (1971), Laneville & Parkinson (1971), and Parkinson (1989) from which the following summary is derived.

A galloping instability that starts from rest (soft galloping) is found to occur for rectangular shapes where the depth-to-height ratio d/h lies between 0·75 and 3, approximately. The basic excitation mechanism for the galloping behaviour is explained from the way in which the shear layers that separate from the front corners, interact with the surfaces of the side faces. The ratio d/h, or more generally the shape of the afterbody, evidently plays an important role in this. For a small positive (i.e. clockwise) angle of attack, the curvature of the lower shear layer will be stronger than that of the upper shear layer, so that the induced pressure on the lower side is lower than that on the upper side. A downward force results which induces the galloping instability. At a certain angle of attack, the lower shear layer attaches on the surface, which is accompanied by a rise in the side pressure which counteracts the suction effect mentioned earlier. Hence, at larger angles the (downward) side force decreases in magnitude and eventually becomes directed upward. This limits the galloping instability and leads to a limit-cycle oscillation. The galloping effect is evidently confined to a smaller range of angles when the rectangle becomes longer, as flow reattachment takes place earlier then. For sufficiently large d/h, the shear layers attach already at the symmetrical orientation, i.e. with $\alpha = 0$, and hence the galloping tendency disappears altogether. For short rectangles, on the other hand, the galloping mechanism is absent at small angles of attack, because the upper and lower shear flows can communicate through the wake region. This adjusts the pressure difference and instead a small upward force results. At larger angles the interaction of the lower shear layer with the side face can suppress this pressure adjustment and the galloping instability returns (hard galloping).

6.2. Quasi-Steady and Unsteady Flow Aspects

In order to identify possible defects of the quasi-steady modelling, it may be worthwhile to consider the results of the unsteady airfoil theory. This comparison is purely for illustrative purposes, as it should by no means be assumed that the airfoil theory can be applied to separated flows. The airfoil theory displays nonseparated flow, where the circulation is determined by the Kutta condition, for which no equivalence exists in separated flow. Bearing this in mind, if the rectangular cylinder model were to be replaced by a thin wing, the unsteady wind loads can be written in the present notation as

$$c_M = C(k)\,\bar{c}_{M_\alpha}\,\alpha + c_{M_\kappa}\frac{d}{R}\frac{\dot{\theta}}{u}. \tag{37}$$

The first term is the circulatory lift contribution, with $\bar{c}_{M_\alpha}$ the static force derivative and α the effective, dynamic angle of attack, for which

$$\bar{c}_{M_\alpha} = 2\pi\left(1+\frac{d}{4R}\right) \approx 2\pi, \qquad \alpha = \theta - \left(1-\frac{d}{4R}\right)\frac{\dot{\theta}}{u} \approx \theta - \frac{\dot{\theta}}{u}. \tag{38}$$

These expressions reflect the classic airfoil results that the steady lift-slope is equal to 2π, with the lift acting at the quarter-chord point, and the angle of attack determined by the effective upwash velocity at the three quarter-chord point. The effect of these exact positions is seen to become unimportant when d/R is small, as is the case for the present configuration ($d/4R = 0{\cdot}03$). Anyway, as these results are specific to the airfoil theory, they should not be expected to have any direct meaning for separated flow. The function $C(k)$ represents Theodorsen's function, which describes the fluid memory effect.

The second term in equation (37) is a dynamic curvature effect. For the airfoil $c_{M_\kappa} = \pi/2$, hence of the same order of magnitude as the lift-slope ($c_{M_\kappa}/\bar{c}_{M_\alpha} = \frac{1}{4}$).

As mentioned, the airfoil results are not directly transferrable to the separated flow around a beam with a rectangular cross-section, but they serve to reveal a number of mechanisms that may be addressed in a critical assessment of the quasi-steady modelling that has been applied in the present case, (cf. Nakamura & Mizota 1975).

6.2.1. *Dynamic curvature*

Firstly, consider only the dynamic curvature effect, which results from the variation of the angle of attack over the cross-section. For the thin wing, where c_{M_κ} is constant, it contributes only to the damping and not to the stiffness, because of its direct dependence on $\dot{\theta}$,

$$c_\zeta = \frac{1}{2}\left(\bar{c}_{M_\alpha} - c_{M_\kappa}\frac{d}{R}\right), \qquad c_k = -\frac{1}{2}\,\bar{c}_{M_\alpha}, \tag{39}$$

while in addition there is no effect of u. For the wing this contribution would be negligible when d/R is small, as in the present configuration. It is indeed this consideration which suggests, as stated in the Introduction, that the quasi-steady approach is in general expected to possess better validity here, than it would for torsional rotations where d and R are of the same order of magnitude. However, a significant net effect can remain even for small d/R, if the sensitivity of the cross-section to dynamic curvature were large. Steinman (1950) suggested that this effect could be determined experimentally by measurement of the steady flow around a curved model, but such a concept may not necessarily be valid for separated flow (Nakamura & Mizota 1975). Although in absence of direct evidence, a number of reasons can be mentioned in support of why the rectangular section would display a larger

curvature sensitivity than the square cross-section, apart from a direct geometrical consideration, i.e. the slenderness of the cross-section. As mentioned in the preceding section, the galloping tendency disappears for longer cross-sections, so that the rectangular cross-section is evidently closer to the critical geometry. Also, experiments on a 2 : 1 cross-section revealed a much stronger sensitivity to free stream turbulence than for a square cross-section (Laneville & Parkinson 1971). Finally, notwithstanding the large deviations for intermediate angles, reasonable agreement is again found for larger angles, for which the damping decreases. A possible reason may be that the flow is especially sensitive to curvature as long as there is an interaction of the shear layers with the side faces, but that this sensitivity disappears when firm reattachment of the shear layers has taken place.

So, in summary, the fact that the damping is affected but not the stiffness, the sensitivity to the cross-sectional shape and its relative independence of u, make this curvature effect a likely candidate to explain the deviations from theory that are observed at these moderate wind speeds. Further research, either experimental or by means of advanced numerical flow simulation, will be required to validate this, and investigate the responsible physical mechanisms.

Note that this curvature effect is absent in translational galloping. Therefore, the corresponding deviation would not be observed in that type of galloping, although the author does not know of such a study of a rectangular cross-section with similar detail in the comparison of experiment and quasi-steady theory as Parkinson's investigation of the square section (Parkinson & Smith 1964).

6.2.2. *Fluid memory*

The fluid memory effect expresses the influence of vorticity in the wake, and is also referred to as the circulation lag effect. Qualitatively, it can be explained as follows. If by a change in α the circulation (and hence the lift) of the body changes, vorticity of opposite sign is shed into the wake, upon which it is convected downstream. At the body, this wake vorticity induces an additional vertical velocity and, hence, changes the effective angle of attack. The oscillation frequency determines the strength and periodicity of the wake vortex system. In airfoil theory this is described as in equation (37) by Theodorsen's function $C(k)$, where k is the reduced frequency, based on the semi-chord. With our present notation, k is related to u as $k = d/(2Ru)$. For the geometry under consideration this yields a value of $k = 0{\cdot}01$ at $u = 5$. The value of k and hence the fluid memory effect evidently increases when lower values of u occur. For the airfoil the consequence of the fluid memory effect is that the wake vorticity results in an attenuation and a phase delay of the aerodynamic forces (or, alternatively, of the effective α) with respect to the quasi-steady results in which the wake effect has been discarded. The lag effect can be illustrated qualitatively by elaborating the vorticity shedding concept. With $\bar{c}_{M_z}$ positive, an increase in α is accompanied by a shedding of negative vorticity which reduces the effective α, while a decrease in α has the opposite effect. Hence, a delay results.

An attenuation of the effective value of α can explain why the galloping amplitudes at low values of u are higher than predicted, as a given value of the *effective* $\hat{\alpha}$ would then require a larger value of $\hat{\theta}$. However, if this were the only relevant mechanism, an overall attenuation would evidently also reduce the level of the damping effect, whereas in contrast it is seen to be amplified. Also, from the shape of the curves, there appears to be no significant shift to larger values of α in general (e.g. the peak position remains near $\alpha = 8^\circ$), as would be consistent with the notion of an overall attenuation effect on α.

If the lag influence of the fluid memory effect can be interpreted as a simple phase delay of α with respect to the quasi-steady case, it can be seen to increase the phase shift angle

ϕ between α and the deflection angle θ, see equation (6), and which is related to u by equation (7) according to the quasi-steady approximation. When the nonlinear force characteristic is approximated by an average value of its slope, $\bar{c}_{M_z}$, it follows directly from the definitions, equations (16) and (17), that the aerodynamic damping and stiffness coefficients for a constant value of u are proportional to $\sin\phi$ and $\cos\phi$, respectively. An additional delay that increases the value of ϕ would thus augment the damping but weaken the stiffness effect. As with decreasing wind speed, the observed deviations in the damping become larger, whereas the increased value of ϕ reduces the sensitivity to a delay, this would require the delay itself to increase significantly. The first argument, however, is in clear contrast to the experimental observation at $u = 4.4$ (with $\phi = 13^\circ$), where both damping and stiffness effect are seen to be amplified significantly. Moreover, if the vorticity mechanism used to illustrate the lag effect for the airfoil is applied to a body with a negative value of $\bar{c}_{M_z}$, a reversed lag effect would result, that is, a reduction instead of an increase of the phase angle ϕ. This leads to the conclusion that as yet there is no obvious explanation of how the fluid memory effect can be responsible for the observed trends at low wind speeds.

Finally, note that when ϕ is small (hence, at large u), a small variation in the phase lag would affect only the damping but hardly the stiffness. So, the observed variations at higher velocities can perhaps be the result of small amplitude-dependent phase shifts in the aerodynamic response.

6.2.3. *Vortex resonance*

Another mechanism which could affect the validity of the quasi-steady approach is the influence of the periodic vortex-shedding. This effect is predominant in vortex-resonance phenomena and may interact with the galloping instability (Novak 1971; Parkinson 1989; Nakamura & Hirata 1994), but in the experiments, a low natural oscillation frequency has been chosen for the very reason of reducing these effects as much as possible. Detailed experiments on the translational motion of a rectangular cross-section with $d/h = 2$ showed good agreement with quasi-steady theory for $U/f_0 h > 20$ for oscillation amplitudes up to $0{\cdot}2h$ (Washizu *et al.* 1978), which corresponds to $u > 0{\cdot}3$ and $\hat{\alpha} < 4^\circ$ in the present notation. These experiments also reveal that there is a trend that the velocity region of vortex-resonance expands when the oscillation amplitude relative to the cylinder height increases, but it does not extend to the high level of amplitudes that occur in the present investigation. Hence, there is no direct evidence as to whether this amplitude effect, possibly in combination with the influence of rotation, can explain the results found here.

6.2.4. *Reynolds number effects*

In addition to these unsteady flow aspects, an explanation for the deviations at low wind speeds may be sought in steady flow effects, notably the influence of the Reynolds number. As an indirect effect, an increase in the boundary layer thickness on the sidewalls of the wind tunnel at low wind speeds would amplify the blockage effect, with respect to the wind speed at which the steady force measurements were obtained. This will certainly tend to increase the forces, and hence both the damping and stiffness effect, but not to such a large extent as observed. This is confirmed by a comparison with steady force measurements obtained in a much larger wind tunnel where the blockage effect is virtually absent. Moreover, this revealed that the blockage effect would tend to reduce the galloping amplitude rather than augment it.

Secondly, there is the possibility of a direct Reynolds number effect; that is, a change in the flow structure around the rectangular beam model itself. In the present configuration,

there is no possibility to obtain direct force data at these low wind speeds, but a numerical flow simulation may be worthwhile to investigate if such an effect indeed occurs. However, comparison between experiments with two square cross-sections of different size seems to indicate that the effect is slightly stronger for the larger diameter. This would not be in support of such a direct Reynolds number effect.

7. CONCLUSIONS

The galloping behaviour of a prismatic beam with a rectangular cross-section has been investigated. This beam performs a motion with a single rotational degree of freedom. For this particular geometry, the effect of the unsteady aerodynamic forces can be explained as a combination of aerodynamic stiffness and damping terms, the latter being the most relevant for the instability behaviour. A theoretical prediction of both damping and stiffness effects for this type of galloping behaviour has been made, based on a quasi-steady modelling of the aerodynamic forces and which employs steady force data obtained from wind tunnel tests. The validity of the quasi-steady approach is suggested by the low value of the natural frequency of the oscillation, in order to avoid vortex-resonance effects, and by taking the rotation arm large with respect to the diameter of the cross-section. This quasi-steady theory predicts that, as long as no significant nonlinear distortion of the oscillation mode occurs, the damping and stiffness effects are a function only of the aerodynamic amplitude of the oscillation, and exactly opposite in sign, i.e. $c_\zeta(\hat{\alpha}) = -c_k(\hat{\alpha})$. Hence, at the amplitude for which the aerodynamic damping is zero, the stiffness effect vanishes as well. As a result, when assuming a low level of structural damping, the limit-cycle oscillation takes place at nearly the natural oscillator frequency, even at moderate wind velocities at which the stiffness effect is significant. This agrees very well with the experiments.

Dynamic wind tunnel tests were carried out to investigate the galloping behaviour of the oscillator and in general reasonable agreement was found with the predictions. However, a number of significant deviations from the quasi-steady predictions were observed, in particular for the damping effect. At moderate wind levels the stiffness effect is in good agreement with theory, whereas significant deviations are observed for the damping effect. Comparison with experiments on a square section suggests that this effect may be affected by the shape of the cross-section, and could possibly be caused by an increased sensitivity to dynamic curvature. Additional deviations from theory were found to occur for low wind speeds, with values of the reduced wind speed u below 5, which had also been found for the square section. Further study is required to investigate whether this is to be attributed to a basically steady flow effect in the experiment (Reynolds number), or that unsteady flow effects are responsible for this, such as the influence of vortex shedding or wake vorticity.

REFERENCES

Blevins, R. D. 1990 *Flow Induced Vibrations*, 2nd edition. New York: Van Nostrand Reinhold.

Dowell, E. H. (ed.), Crawley, E. F., Curtiss, H. C., Peters, D. A., Scanlan, R. H. & Sisto, F. 1995 *A Modern Course in Elasticity*, 3rd edition. Dordrecht: Kluwer Academic Publishers.

Guckenheimer, J. & Holmes, P. 1990 *Nonlinear Oscillations, Dynamical Systems and Bifurcations of Vector Fields*. New York: Springer-Verlag.

Haaker, T. I. & van Der Burgh, A. H. P. 1994 On the dynamics of aeroelastic oscillators with one degree of freedom. *SIAM Journal of Applied Mathematics* **54,** 1033–1047.

Haaker, T. I. & van Oudheusden, B. W. 1997 One-degree-of-freedom rotational galloping under strong wind conditions. *International Journal of Non-Linear Mechanics* **32,** 803–814.

LANEVILLE, A. & PARKINSON, G. V. 1971 Effects of turbulence on galloping of bluff cylinders. In *Proceedings Third International Conference Wind Effects on Buildings and Structures*, Tokyo, pp. 787–797.

MODI, V. J. & SLATER, J. E. 1974 Quasi-steady analysis of torsional aeroelastic oscillators. *Proceedings IUTAM-IAHR Symposium Flow-Induced Structural Vibrations*, Karlsruhe, 1972, pp. 355–372, Berlin: Springer-Verlag.

NAKAMURA, Y. & HIRATA, K. 1989 Critical geometry of oscillating bluff bodies. *Journal of Fluid Mechanics* **208,** 375–393.

NAKAMURA, Y. & HIRATA, K. 1994 The aerodynamic mechanism of galloping. *Transactions of the Japan Society for Aeronautical and Space Sciences* **36,** 257–269.

NAKAMURA, Y. & MIZOTA, T. 1975 Torsional flutter of rectangular prisms. *ASCE Journal of the Engineering Mechanics Division*, **101,** 125–142.

NOVAK, M. 1971 Galloping and vortex induced oscillations of structures. *Proceedings of the Third International Conference Wind Effects on Buildings and Structures*, Tokyo, pp. 799–809.

PARKINSON, G. V. & SMITH, J. D. 1964 The square prism as an aeroelastic nonlinear oscillator. *Quarterly Journal of Mechanics and Applied Mathematics* **17,** 225–239.

PARKINSON, G. V. 1989 Phenomenon and modelling of flow-induced vibrations of bluff bodies. *Progress in Aerospace Sciences* **26,** 169–224.

STEINMAN, D. B. 1950 Aerodynamic theory of bridge oscillations. *Transactions of the ASCE* **116,** 1180–1217.

VAN OUDHEUSDEN, B. W. 1995 On the quasi-steady analysis of one-degree-of-freedom galloping with combined translational and rotational effects. *Nonlinear Dynamics* **8,** 435–451.

VAN OUDHEUSDEN, B. W. 1996a Rotational one-degree-of-freedom galloping in the presence of viscous and frictional damping. *Journal of Fluids and Structures* **10,** 673–689.

VAN OUDHEUSDEN, B. W. 1996b Aerodynamic stiffness effects in rotational galloping at high wind speeds. *Journal of Wind Engineering and Industrial Aerodynamics* **64,** 31–46.

VAN OUDHEUSDEN, B. W. 1998 Investigation of large-amplitude 1-DOF rotational galloping. *Series* 01: *Aerodynamics* 03. Delft: Delft University Press, ISBN 90-407-1566-1.

WASHIZU, K., OHYA, A., OTSUKI, Y. & FUJI, K. 1978 Aeroelastic instability of rectangular cylinders in a heaving mode. *Journal of Sound and Vibration* **59,** 195–210.

APPENDIX A: THE DETERMINATION OF THE STRUCTURAL DAMPING

In the analysis of the dynamic oscillation behaviour in the main text, only viscous damping was considered, where the damping force is proportional to the angular displacement velocity, and the level of which is controlled by means of the inductive damper. For the experiments the actual amount of structural damping was determined from free-decay oscillation test of the set-up. Detailed analysis of the results revealed that also small amounts of frictional and quadratic damping could be identified, i.e. with damping force components being, respectively, constant or quadratically dependent on the angular velocity. The first component typically corresponds to the so-called Coulomb (dry) friction, notably present in the bearings of the angle encoder, while the quadratic term can be traced in particular to the aerodynamic drag of the oscillator moving in still air.

Including these effects, the equation of motion as given by equation (20), now reads

$$\ddot{\theta} + \Omega^2\theta = -\left(2\zeta_0\dot{\theta} + \frac{\pi}{2}\,C_1\,\mathrm{sgn}(\dot{\theta}) + \frac{3\pi}{4}\,C_2\dot{\theta}|\dot{\theta}|\right) + \mu u^2 c_M, \tag{A1}$$

relating to a harmonic oscillation at an angular frequency $\omega = \Omega\omega_0$, i.e. for the system with additional stiffness effects included. The parameters C_1 and C_2 are the coefficients of frictional and quadratic damping, respectively, where the factors $\pi/2$ and $3\pi/4$ have been included for normalization.

Upon averaging the following amplitude-transient equation is then obtained, cf. equation (22),

$$\frac{\mathrm{d}\hat{\theta}}{\mathrm{d}\tau} = -\left((\zeta_0 + \mu u c_\zeta)\hat{\theta} + \frac{C_1}{\Omega} + C_2\Omega\hat{\theta}^2\right). \tag{A2}$$

For the strong-forcing analysis, the stability of the oscillation is obtained from equation (31), which now becomes

$$\frac{\mathrm{d}}{\mathrm{d}\tau} H_s = -\left((\zeta_0 + \mu u c_\zeta) \langle 2\dot{\theta}^2 \rangle + C_1 \left\langle \frac{\pi}{2} |\dot{\theta}| \right\rangle + C_2 \left\langle \frac{3\pi}{4} |\dot{\theta}^3| \right\rangle \right). \tag{A3}$$

The calculation of the aerodynamic damping coefficient c_ζ from time-record data, comparable to equation (36), now involves evaluation of equation (A2), and is

$$c_\zeta = -\frac{1}{\mu u} \left(\frac{1}{\hat{\theta}} \frac{\mathrm{d}\hat{\theta}}{\mathrm{d}\tau} + \zeta_0 + \frac{C_1}{\hat{\theta}\Omega} + C_2 \hat{\theta}\Omega \right). \tag{A4}$$

For limit-cycle oscillations evidently the decay rate term vanishes from the expression, cf. equation (35). Note the frequency effect of Ω in the nonviscous damping terms.

In order to determine the values of the structural damping coefficients, the amplitude decay of free oscillations was observed. In that case, with $\Omega = 1$ and $u = 0$, equation (A2) gives

$$\frac{\mathrm{d}\hat{\theta}}{\mathrm{d}\tau} = -(\zeta_0 \hat{\theta} + C_1 + C_2 \hat{\theta}^2). \tag{A5}$$

Hence, the damping coefficients ζ_0, C_1 and C_2 can be obtained from a quadratic fit of the experimentally determined amplitude decay rate. This is illustrated in Figure A1, where the decay rate is plotted versus the amplitude, for five different damper settings (the lowest setting is with the damper inactive). The curves represent the results of a least-squares quadratic fit to the data, corresponding to the values of the damping parameters in Table A1. The concept that the inductive damper introduces only viscous damping, whereas the frictional and quadratic damping effects remain constant, is in good agreement with the findings in the table, where C_1 and C_2 are essentially constant, apart from C_2 at the highest damping level.

As mentioned, the quadratic damping effect can be (partly) related to the aerodynamic drag on the oscillator components. This includes the drag of the cylinder model inside the wind tunnel, which should however be excluded from the structural damping, as during the galloping tests the forces on the cylinder are modelled explicitly. The effect of the cylinder

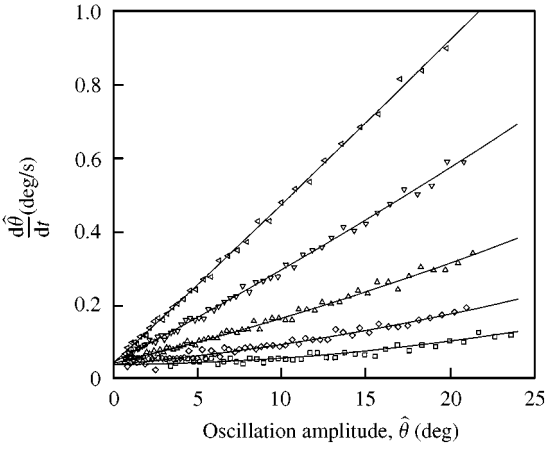

Figure A1. Characterization of the structural damping from amplitude decay rate measurements.

TABLE A1
Experimental damping parameters

Damper setting	ζ_0	C_1 (deg)	C_2 (1/deg)
"0"	0·0002	0·0091	0·000033
"1"	0·0011	0·0098	0·000036
"2"	0·0028	0·0107	0·000034
"3"	0·0062	0·0114	0·000032
"4"	0·0109	0·0108	0·000017

drag in the free-decay tests can be estimated to contribute to C_2 by the following amount:

$$(\Delta C_2)_{\text{cylinder}} = \frac{4}{3\pi}\,\mu C_D(\text{rad}^{-1}) = \frac{1}{135}\,\mu C_D\,(\text{deg}^{-1}).$$

With the mass parameter $\mu = 0{\cdot}0013$ and the cylinder drag coefficient estimated at $C_D \approx 2$, this yields a contribution to C_2 of about $0{\cdot}00002\ \text{deg}^{-1}$, which is of the order of half the total value measured. In the subsequent analysis of the data, this effect was compensated for in first approximation, by reducing the value of the quadratic component of the structural damping, to a constant value of $C_2 = 0{\cdot}00001\ \text{deg}^{-1}$.

APPENDIX B: NOMENCLATURE

b cylinder span
c_k aerodynamic stiffness coefficient, defined in equation (15)
c_M oscillator moment coefficient, $2M/\rho U^2 dbR$
c_ζ aerodynamic damping coefficient, defined in equation (15)
d cylinder depth (= streamwise dimension)
f frequency
h cylinder height (= cross-flow dimension)
I moment of inertia
k restoring force stiffness
M aerodynamic moment around oscillator rotation axis
R oscillator arm length
t time
U wind speed
u reduced wind speed, $U/\omega_0 R$
α angle of attack
ε aerodynamic forcing parameter, μu^2
ζ_0 viscous damping coefficient
θ rotational oscillator displacement
μ mass parameter, $\rho dbR^3/2I$
ρ air density
τ nondimensional time, $\omega_0 t$
ω radial frequency, $2\pi f$
Ω frequency ratio, ω/ω_0